

# WAVELET METHODS FOR THE REPRESENTATION, ANALYSIS AND SIMULATION OF OPTICAL SURFACES

PHILIPP JESTER<sup>†‡</sup>, CHRISTOPH MENKE<sup>†</sup>, AND KARSTEN URBAN<sup>‡</sup>

**Abstract.** In this paper, we introduce a wavelet method for the description, approximation, analysis and simulation of optical surfaces. We describe the new method and show results of several numerical experiments for relevant applications in optics.

We focus on three main aspects. First, we describe a highly accurate representation of smooth optical surfaces in terms of a B-spline quasi-interpolant. This representation is used in a ray trace algorithm for the analysis of optical systems and is particularly suited for a wavelet decomposition. The Fast Wavelet Transform gives access to the use of wavelets for the separation of low and mid spatial frequency errors modeled by Zernike polynomials and Power Spectral Density functions, as well as the localization and correction of errors. We compare our results with the classical representation in terms of Zernike polynomials.

**Key words.** optical system, wavelets, ray tracing, error analysis

**AMS subject classifications.** 42C40, 78A10, 65T60

**1. Introduction.** The shape of optical surfaces ranges from flat surfaces and spherical sections to rotationally symmetric surfaces with mild or strong deviation from a best-fit sphere to freeform surfaces with or without symmetries. Because they are easily manufactured, flat and spherical surfaces are by far the most common. These surfaces can be described by just one parameter, i.e., the curvature of the surface. Advances in fabrication technology and optical design led to a regular use of aspheric elements in optical systems. Aspheric surfaces are often described in terms of a power series expansion of a basic conical section.

The evaluation of the performance of optical systems is usually based on ray trace algorithms. In order to determine the path of a ray through an optical system, the intersection points of the ray with the optical surfaces have to be computed. For an optical system that contains only spherical surfaces, this calculation is straightforward and an analytical expression can be given. In general, there exists no analytical expression and iterative procedures have to be used to calculate approximations for the intersection points.

In some cases, the representation of a surface in terms of polynomials turned out to be impractical. Freeform surfaces without symmetries that are frequently used in illumination systems may fall into this category. Another example is the description of an aspheric surface as it is built including manufacturing errors.

Usually the surfaces show high-frequency oscillations and local defects due to imperfections in the tools and the manufacturing process. Trying to represent such an as-built surface by polynomials inevitably leads to a high number of terms and makes ray tracing expensive and time-consuming. In addition, if local structures are present on the surface, a large approximation error is introduced despite of the high number of polynomial terms in a global representation of the surface. Consequently there is a need for alternative surface descriptions that combine high approximation accuracy with fast evaluation.

---

<sup>†</sup>Carl Zeiss AG, Corporate Research and Technology, Carl-Zeiss-Str. 22, 73447 Oberkochen, Germany.

<sup>‡</sup>University of Ulm, Institute for Numerical Mathematics and Scientific Computing Center Ulm (UZWR), 89081 Ulm, Germany.

One possibility is the use of the well-known Zernike polynomial system not only for the characterization of the wave front but also for the description of the surface [11]. These functions are often used to establish a direct connection between surface defects and the aberrations of the optical system. However, a global description by Zernike polynomials is not well-suited for the representation of local structures on subapertures of a surface.

Several authors considered alternative aspheric representations. Greynolds [10] gives a brief review of the so-called ‘superconic’ and ‘subconic’ surface descriptions. The motivation for the introduction of these types was to produce steep aspheres with less terms and smoother correction. Recently, Forbes [8] proposed a sum of Jacobi polynomials to represent rotationally symmetric aspheres. These polynomials constitute an orthonormal basis of the unit circle. Forbes’ representation has the property to facilitate the enforcement of fabrication constraints, e.g. the deviation of the slope from a best-fit sphere. For non-rotationally symmetric surfaces, splines have been studied in the literature [9, 17, 18]. Parametric curves such as non-uniform rational B-splines (NURBS) have been applied to the design of rotationally symmetric aspheres [3] as well as to the design of freeform mirrors [16]. Because NURBS are a standard surface type in CAD software, they offer an attractive surface description when data has to be exchanged between optical design and CAD tools. Another optical surface representation using 2D Gaussians as radial basis functions has been introduced by Cakmakci and co-workers [2]. The emphasis of their work is a surface description that is suitable for the optimization of rotationally symmetric as well as freeform systems. They represent an optical surface as a sum of 2D Gaussians as basis functions. Gaussians are smooth functions having derivatives of all orders and can be regarded as local functions. The Fourier transform of a Gaussian is again a Gaussian which gives access to the Power Spectral Density (PSD) function of the surface. Therefore, Gaussians have several desirable properties in the context of optical design.

Wavelets are a class of functions used to localize a given signal in both frequency and space domains [4, 21]. An arbitrary function is represented as a linear combination of local basis functions. The basis functions are obtained from a single prototype wavelet, called the mother wavelet, by scaling (dilation) and shifting (translation). The localization property of (compactly supported) wavelets offers a unique advantage over Fourier methods for detecting local spatial structures. In signal analysis and image processing wavelet methods are a well-established tool [14]. Wavelet transforms have also been used in the analysis of surface data [7]. Recently, Tien and Lyu introduced an inspection method based on the discrete wavelet transform [19]. Their method offers fast and automated recognition of surface defects and deformations for manufactured optical surfaces with flat shape.

Because wavelets are well adapted to represent both local and global structures, a wavelet approach to the representation of optical surfaces seems promising. We restrict ourselves to non-diffractive elements and assume sufficiently smooth surfaces. Refraction and reflection of a ray at a surface are calculated with the surface normal at the intersection point. This means that we have to evaluate the derivative of the surface function during the ray trace algorithm. To facilitate this, we use cardinal B-splines as basis functions. They offer the advantage that a recursive formula exists for themselves as well as for their derivatives.

The surface data is contained in a bounding box. In order to obtain an accurate approximation, a quasi-interpolation is applied. As we will see, this reduces to a

weighting of the data in the case of B-spline basis functions. We present a ray trace algorithm using this surface description. The iterative calculation of the intersection points is performed by a Newton method. This implementation of a ray tracing allows the evaluation of the performance of optical systems using measured surface data as well as tolerating surface errors in different spatial frequency regimes.

A wavelet approach is also appropriate for the analysis of optical surfaces. We apply a fast wavelet transformation (FWT) to measurement data to obtain a wavelet representation. Threshold algorithms that cut the wavelet coefficients are used to separate noise introduced by the measurement from the underlying structures of the surface. The reconstruction of the manipulated data is performed by the inverse FWT.

This paper is organized as follows. In §2, we collect the main facts of B-spline multiresolution and wavelets that are relevant for this paper. A short introduction how to model surface errors in optics is given in §3. Section 4 is devoted to the B-spline quasi-interpolation method with corresponding numerical results also for the ray tracing in §5 and §6. We describe and test our wavelet method in §7. The paper ends with a summary and outlook.

**2. B-Splines and Multiresolution.** We start by reviewing those basic facts on B-splines, Multiresolution Analysis (MRA) and wavelets that will be relevant in the sequel.

We recall only the main facts of B-splines and refer to [6] for details. There are several equivalent definitions of *cardinal B-splines*  $N_d$ , we use the following recursive scheme

$$N_1(x) := \chi_{[0,1)}(x), \quad N_d(x) := \int_0^1 N_{d-1}(x-t) dt = (N_{d-1} * N_1)(x),$$

for  $d \geq 1$ . The following properties are well-known and will frequently be used in the sequel

$$\text{supp } N_d \subset [0, d] \quad (\text{locality}), \quad (2.1)$$

$$N_d(x) = \frac{x}{d-1} N_{d-1}(x) + \frac{d-x}{d-1} N_{d-1}(x-1) \quad (\text{recursion}), \quad (2.2)$$

$$N_d \in C^{d-2}(\mathbb{R}) \text{ with } N'_d(x) = N_{d-1}(x) - N_{d-1}(x-1) \quad (\text{regularity}). \quad (2.3)$$

Note that (2.2) offers a fast recursive evaluation procedure since the evaluation is trivial for  $N_1$ . In addition (2.3) also allows a fast evaluation of derivatives. Another important property of  $N_d$  is the following equation

$$N_d(x) = 2^{1-d} \sum_{k=0}^d \binom{d}{k} N_d(2x-k), \quad x \in \mathbb{R},$$

which is known as *refinement equation*. Finally, it is known that shifts of  $N_d$ , i.e.  $N_d(\cdot - k)$ ,  $k \in \mathbb{Z}$ , are linearly independent. These last two properties mainly enable B-splines to generate a Multiresolution Analysis (MRA) which will be described next. We define for a piecewise continuous function  $g : \mathbb{R} \rightarrow \mathbb{R}$  its scaled and shifted variant as  $g_{j,k}(x) := 2^{j/2} g(2^j x - k)$ , where  $j \in \mathbb{Z}$  is called level,  $k \in \mathbb{Z}$ . Next, abbreviating  $\varphi := N_d$  and  $S_j := \text{clos}_{L_2(\mathbb{R})} \Phi_j$ ,  $\Phi_j := \{\varphi_{j,k} : k \in \mathbb{Z}\}$ , we obtain the

following properties

$$S_j \subset S_{j+1} \quad (\text{nestedness}), \quad (2.4a)$$

$$\text{clos}_{L_2(\mathbb{R})} \bigcup_{j \in \mathbb{Z}} S_j = L_2(\mathbb{R}), \quad \bigcap_{j \in \mathbb{Z}} S_j = \{0\} \quad (\text{span and intersection}), \quad (2.4b)$$

$$f \in S_j \iff f(2 \cdot) \in S_{j+1} \quad (\text{scaling}), \quad (2.4c)$$

$$f \in S_0 \iff f(\cdot - k) \in S_0 \quad (\text{shift invariance}), \quad (2.4d)$$

$$\Phi_j \text{ is a Riesz basis for } S_j \text{ with constants independent of } j. \quad (2.4e)$$

A sequence  $\mathcal{S} = \{S_j\}_{j \in \mathbb{Z}}$  of spaces satisfying (2.4) is called *Multiresolution Analysis (MRA)* [14] and the function  $\varphi$  *scaling function* of the MRA. There are also other functions than  $N_d$  satisfying (2.4). Here, we are only interested in compactly supported generators  $\varphi$ . One can show that (2.4) implies the existence of a dual scaling function  $\tilde{\varphi}$  such that

$$(\varphi(\cdot), \tilde{\varphi}(\cdot - k))_{0; \mathbb{R}} = \delta_{0, k}, \quad k \in \mathbb{Z},$$

and  $\tilde{\varphi}$  generates a dual MRA  $\tilde{\mathcal{S}}$ . We denote by  $(u, v)_{0; \Omega}$  the inner product on  $L_2(\Omega)$  and the induced norm by  $\|u\|_{0; \Omega} := \sqrt{(u, u)_{0; \Omega}}$ . There exist several  $\tilde{\varphi}$  labelled by an index  $\tilde{d}$ ,  $d + \tilde{d}$  even, and denoted by  $\tilde{N}_{d, \tilde{d}}$ . This additional index has the following meaning: Whereas  $N_d$  are piecewise polynomials (and each polynomial  $p \in \mathcal{P}_{d-1}$  can be represented by  $\Phi_0$ ), we obtain that

$$x^r = \sum_{k \in \mathbb{Z}} \alpha_{r, k} \tilde{\varphi}(x - k), \quad \alpha_{r, k} := \int_{\mathbb{R}} t^r \varphi(t - k) dt,$$

for  $0 \leq r \leq \tilde{d} - 1$ . Moreover, also  $\tilde{N}_{d, \tilde{d}}$  are compactly supported [5].

Given a scaling function  $\varphi$ , the biorthogonal projection  $P_j : L_2(\mathbb{R}) \rightarrow S_j$  of a function  $f \in L_2(\mathbb{R})$  onto the space  $S_j$  is given by

$$P_j f = \sum_{k \in \mathbb{Z}} (f, \tilde{\varphi}_{j, k})_{0; \mathbb{R}} \varphi_{j, k}. \quad (2.5)$$

If  $\Phi_j$  represents polynomials in  $\mathcal{P}_{d-1}$  (up to degree  $d-1$ ), the following error estimate is well-known

$$\|f - P_j f\|_{0; \mathbb{R}} \lesssim 2^{-js} \|f\|_{s; \mathbb{R}}, \quad f \in H^s(\Omega), \quad 0 \leq s < d.$$

Here,  $A \lesssim B$  means that  $A \leq cB$  with a uniform constant  $c > 0$ . Moreover,  $H^s(\Omega)$  denotes the standard Sobolev norm of weakly differentiable functions of order up to  $s \in \mathbb{N}$  normed by

$$\|f\|_{s; \mathbb{R}}^2 := \sum_{m=0}^s \|\partial^m f\|_{0; \mathbb{R}}^2.$$

There is also a generalization to  $s \in \mathbb{R}^+$ . We will use periodic scaling functions in the sequel. To this end, we define the periodization of a continuous function  $f : \mathbb{R} \rightarrow \mathbb{R}$  by

$$[f](x) := \sum_{k \in \mathbb{Z}} f(\cdot - k)|_{[0, 1]}(x).$$

Then,  $\varphi_{j,k} := [\varphi]_{j,k}$  gives rise to a system of linearly independent functions  $\Phi_j := \{\varphi_{j,k} : k \in \mathcal{I}_j\}$ ,  $\mathcal{I}_j := \{0, \dots, 2^j - 1\}$ , that span nested spaces  $S_j$  of periodic functions. In other words,  $[\varphi]$  is a generator of a periodic MRA.

Now, we introduce biorthogonal wavelets. Let two MRA's  $\mathcal{S}, \tilde{\mathcal{S}}$  generated by scaling functions  $\varphi, \tilde{\varphi}$  be given and define complement spaces  $W_j, \tilde{W}_j$  by

$$S_{j+1} = S_j \oplus W_j, \quad \tilde{S}_{j+1} = \tilde{S}_j \oplus \tilde{W}_j, \quad S_j \perp \tilde{W}_j, \quad \tilde{S}_j \perp W_j.$$

A function  $\psi$  is called (*mother*) *wavelet* if

$$\Psi_j := \{\psi_{j,k} : k \in \mathcal{J}_j := \mathcal{I}_{j+1} \setminus \mathcal{I}_j\}$$

is a Riesz basis for  $W_j$  and  $\Psi := \cup_j \Psi_j$  for  $L_2(\mathbb{R})$ . One can show that there is a corresponding dual wavelet  $\tilde{\psi}$ , i.e.,

$$(\psi_{j,k}, \tilde{\psi}_{j',k'})_{0;\mathbb{R}} = \delta_{j,j'} \delta_{k,k'}, \quad j, j', k, k' \in \mathbb{Z}.$$

In addition, we assume that  $\psi, \tilde{\psi}$  are compactly supported, e.g. the Cohen-Daubechies-Feauveau (CDF)-biorthogonal B-spline wavelets [5]. The periodization is straightforward.

One main ingredient for our later application is the *Fast Wavelet Transform* (FWT) described as follows. Let  $f_j \in S_j$ , then

$$f_j = \sum_{k \in \mathcal{I}_j} c_{j,k} \varphi_{j,k}, \quad c_{j,k} := (f_j, \tilde{\varphi}_{j,k})_{0;\mathbb{R}}, \quad \mathbf{c}_j := (c_{j,k})_{k \in \mathcal{I}_j},$$

is called *single scale representation* of  $f_j$ . Since  $S_j = S_{j-1} \oplus W_{j-1}$ , we obtain the alternative representation

$$f_j = \sum_{k \in \mathcal{I}_{j-1}} c_{j-1,k} \varphi_{j-1,k} + \sum_{k \in \mathcal{J}_{j-1}} d_{j-1,k} \psi_{j-1,k}$$

and straightforward calculations show that

$$c_{j-1,m} = \frac{1}{\sqrt{2}} \sum_{k \in \mathcal{I}_j} c_{j,l} \tilde{a}_{l-2m}, \quad d_{j-1,m} = \frac{1}{\sqrt{2}} \sum_{k \in \mathcal{I}_j} c_{j,l} \tilde{b}_{l-2m},$$

where  $\tilde{a}_k, \tilde{b}_k$  are the dual refinement and wavelet coefficients, i.e.,

$$\tilde{\varphi}(x) = \sum_{k \in \mathcal{I}_j} \tilde{a}_k \tilde{\varphi}(2x - k), \quad \tilde{\psi}(x) = \sum_{k \in \mathcal{I}_j} \tilde{b}_k \tilde{\varphi}(2x - k).$$

The mapping  $\mathbf{c}_j \mapsto (\mathbf{c}_{j-1}, \mathbf{d}_{j-1})$  is called *decomposition* and the iterated application

$$\text{FWT} : \mathbf{c}_j \mapsto (\mathbf{c}_0, \mathbf{d}_0, \dots, \mathbf{d}_{j-1})$$

is known as *Fast Wavelet Transform*. It is remarkable that the FWT and also its inverse IFWT both are of linear complexity as long as primal and dual scaling functions are compactly supported. We obtain the wavelet representation of  $f_j \in S_j$  as

$$f_j = \sum_{\ell=-1}^{j-1} \sum_{k \in \mathcal{J}_\ell} d_{\ell,k} \psi_{\ell,k},$$

where we have set  $\psi_{-1,k} := \varphi_{0,k}$ ,  $d_{-1,k} := c_{0,k}$  and  $\mathcal{I}_{-1} := \mathcal{I}_0$  for simplicity. With respect to the single scale projectors  $P_j$  in (2.5) the detail reads

$$Q_j f := (P_{j+1} - P_j)f = \sum_{k \in \mathbb{Z}} (f, \tilde{\psi}_{j,k})_{0;\mathbb{R}} \psi_{j,k}.$$

For a given function  $f \in L_2(\mathbb{R})$ , the term  $(f, \tilde{\psi}_{j,k})_{0;\mathbb{R}}$  is called *wavelet coefficient*.

Finally, we consider the two-dimensional case. It is readily seen that the bivariate tensor product

$$\varphi_{j,\mathbf{k}}^{2D}(x, y) := (\varphi_{j,k_1} \otimes \varphi_{j,k_2})(x, y) = \varphi_{j,k_1}(x) \cdot \varphi_{j,k_2}(y), \quad \mathbf{k} = (k_1, k_2),$$

is refinable and  $\Phi_j^{2D} := \{\varphi_{j,\mathbf{k}}^{2D} : \mathbf{k} \in \mathcal{I}_j^{2D} := \mathcal{I}_j \times \mathcal{I}_j\}$  generates a MRA  $S^{2D}$  in  $L_2(\mathbb{R}^2)$  or  $L_2([0, 1]^2)$  with periodic functions. In the 2D-case, one has 3 different types of wavelets, often referred to as horizontal, vertical and diagonal detail

$$\psi^H := \psi \otimes \varphi, \quad \psi^V := \varphi \otimes \psi, \quad \psi^D := \psi \otimes \psi.$$

Then, single scale and wavelet representation of a function  $f_j \in S_j$  reads

$$f_j = \sum_{\mathbf{k} \in \mathcal{I}_j^{2D}} c_{j,\mathbf{k}} \varphi_{j,\mathbf{k}}^{2D} = \sum_{\ell=-1}^{j-1} \sum_{e \in \{H,V,D\}} \sum_{\mathbf{k} \in \mathcal{I}_\ell^{2D}} d_{\ell,\mathbf{k}}^e \psi_{\ell,\mathbf{k}}^e.$$

The FWT reads similar, again with linear complexity.

Nowadays, there is a deep analysis of wavelets available, several results have been proven and wavelets have been used in different areas. We just mention [21] for a recent monograph. Let us describe one property that is important in the sequel. It is easily seen that polynomial exactness of the dual scaling functions imply vanishing moments of the primal wavelets. That means

$$M_r(\psi) := \int_{\mathbb{R}} x^r \psi(x) dx = 0, \quad 0 \leq r < \tilde{d}.$$

The left term in the equation is called  $r$ -th order moment and a wavelet is said to have vanishing order  $\tilde{d}$  if  $M_r(\psi) = 0$  for all  $0 \leq r < \tilde{d}$ . If  $\psi$  has  $\tilde{d}$  vanishing moments, then it is known that

$$|(f, \psi_{j,k})_{0;\Omega}| \lesssim 2^{-js} \|f\|_{s;\text{supp } \psi_{j,k}}$$

for all  $f \in H^s(\text{supp } \psi_{j,k}) \cap L_2(\Omega)$ , and  $0 \leq s < \tilde{d}$ . This means that wavelet coefficients of a function are small provided the underlying function is *locally* smooth (since  $|\text{supp } \psi_{j,k}| \lesssim 2^{-j}$ ). Vice versa, large wavelet coefficients indicate local non-regularity. With regard to optical surfaces this means that large wavelet coefficients are an indicator for local errors. This is the mathematical foundation for our method.

**3. Errors of Optical Surfaces.** Since decades, Carl Zeiss AG produces high quality optical systems. The demands of modern optical systems require a careful investigation of errors that might be present in such a system. Those errors may result from the production, the assembling or from damages e.g. caused by the transport. Besides the analysis of such errors, the interest lies of course in their correction in order to assure a prescribed specification of an optical system.

Let us restrict ourselves in the following to surface errors of elements of an optical system. Typically, these errors are classified in terms of their spatial frequencies, namely *low*, *mid* and *high spatial frequency perturbations* [12]. Low spatial frequency perturbations are long wave defects, that cause classical aberrations, like astigmatism or coma. In contrast, typical ripple pattern and waviness are usually interpreted as a mid spatial frequency perturbation. This type of surface error may cause a diffusion of light incident on the surface with a small angle range and reduce the resolution of the optical system. Finally, high spatial frequency perturbations characterize polishing defects or micro roughness which leads to a wide angle diffusion of light. This has no effect on the resolution but lowers the contrast and is mainly considered in scattered light calculations. For ray tracing and tolerating these perturbations are negligible, so that we consider only low and mid spatial frequency perturbations here.

Traditionally, the focus in optics lies in the investigation of low frequency errors. These are described by the orthogonal system of *Fringe-Zernike polynomials*  $\{Z_m : m \in \mathbb{R}\}$  that are also used in the characterization of wave front errors [15]. They represent an orthonormal basis on the unit circle and so are well-suited to describe global irregularities of a circular surface or fitting errors. Moreover, these functions do have a physical interpretation which makes them particularly interesting in optics. The corresponding part of the error should be called *ZFR error* and is denoted by

$$err_{\text{ZFR}}(x, y) := \sum_{m=1}^{\infty} c_m Z_m(x, y), \quad c_m \in \mathbb{R}.$$

The properties of the perturbations  $err_{\text{ZFR}}$  are well investigated and their influence on the optical system is well established [12]. The abbreviation ZFR for Fringe-Zernike is standard in optics.

As already mentioned, the demands of high-resolution optical systems enforce the optical industry nowadays also to investigate the mid frequency errors. This is typically modeled by a so-called *Power Spectral Density (PSD)* function. The PSD is a useful tool if one wants to identify oscillatory signals in time series data and to determine their amplitude. The corresponding error is denoted by  $err_{\text{PSD}}$ . Given a PSD  $P$  (for which one chooses a probability density function), the relationship to the corresponding  $err_{\text{PSD}}$  is given by

$$P(\omega_x, \omega_y) := \left| \mathcal{F}[err_{\text{PSD}}(x, y)] \right|^2, \quad (3.1)$$

where  $\omega_x$  and  $\omega_y$  are spatial frequencies and  $\mathcal{F}$  denotes the Fourier transform.

Let us briefly describe a method to realize  $err_{\text{PSD}}$ . We define an equidistant mesh with  $n \times n$  grid points, which coincides with the spatial frequencies  $\omega_x = \omega_y$ . For every grid point, we compute a realization of  $P$  and the phase  $\phi(i, j)$ . This is done by choosing specific probability distributions and using a random number generator for the chosen distribution. Finally, we obtain the surface error  $err_{\text{PSD}}$  by applying the inverse Fourier transform as described above. For a continuous surface we obtain the following representation

$$err_{\text{PSD}}(x, y) = c_0 + \sum_{i,j=0}^{\frac{n-1}{2}} (a_{i,j} \cdot \sin(i\pi x + j\pi y + \alpha_{i,j}) + b_{i,j} \cdot \sin(i\pi x - j\pi y + \beta_{i,j})),$$

with  $c_0 := \frac{\pi}{2} \sqrt{P(0, 0)}$  and Fourier coefficients

$$a_{i,j} := \Delta_{i,j} \sqrt{P(i\pi, j\pi) + P(-i\pi, -j\pi)}, \quad b_{i,j} := \Delta_{i,j} \sqrt{P(i\pi, -j\pi) + P(-i\pi, j\pi)},$$

where  $\Delta_{i,j} := \frac{\pi}{2\sqrt{2}}(2 - \delta_{i,0} - \delta_{j,0})$  and phase values

$$\alpha_{i,j} := \frac{\pi}{2} + \frac{1}{2}(\phi(i\pi, j\pi) - \phi(-i\pi, -j\pi)), \quad \beta_{i,j} := \frac{\pi}{2} + \frac{1}{2}(\phi(i\pi, -j\pi) - \phi(-i\pi, j\pi)).$$

We have chosen  $P \sim \chi_2^2$  with two degrees of freedom and  $\phi \sim U([0, 2\pi))$ , i.e., the uniform distribution. Hence, we have two free parameters left,  $n$  and the scaling of  $err_{\text{PSD}}$ . As already mentioned, we neglect the high frequency part of the error, so we assume that the total error can be represented as  $err_{\text{TOTAL}} := err_{\text{ZFR}} + err_{\text{PSD}}$ .

**4. B-Spline Representation.** In this section, we introduce the description of an optical surface in terms of B-splines. Of course, such an approach is by far not new [9]. However, we will use a more recent quasi-interpolation scheme in order to guarantee the accuracy of the representation and also as a preparation for the later wavelet analysis. The framework under consideration is the following. On one hand, there is a ‘theoretical’ shape of the surface which is a smooth function  $f : \Omega \rightarrow \mathbb{R}$ , describing an ‘optimal’ optical surface, e.g. a sphere, asphere or freeform surface. Here,  $\Omega \subset \mathbb{R}^2$  is a closed and bounded domain e.g. the area that is needed to define the parameterization of the surface. Without loss of generality, we can assume that  $\Omega \subset \square = [0, 1]^2$  with a positive distance of  $\Omega$  to the boundary of the box. In particular, we extend  $f$  to  $\square$ , i.e., we consider  $f : \square \rightarrow \mathbb{R}$ . On the other hand, in many relevant situations, we are just given measurements of a surface in terms of point values. We would like to be able to reconstruct the underlying surface. Moreover, these measurement data are always affected by errors. Hence, the second issue is to analyze and possibly correct such errors.

#### 4.1. Projection and Quasi-Interpolation.

**Projection.** If a surface is given by a function  $f : \square \rightarrow \mathbb{R}$ ,  $f \in L_2(\square)$ , which we assume to be periodic and  $\Psi = \{\psi_{j,\mathbf{k}} : (j, \mathbf{k}) \in \mathcal{J}^{2D}\}$ ,  $\mathcal{J}^{2D} = \cup_{j=0}^{\infty} j \times \{0, \dots, 2^j - 1\}^2$ , is a wavelet basis, then the following representation is well-known

$$f = \sum_{(j,\mathbf{k}) \in \mathcal{J}^{2D}} d_{j,\mathbf{k}} \psi_{j,\mathbf{k}}, \quad d_{j,\mathbf{k}} = (f, \tilde{\psi}_{j,\mathbf{k}})_{0;\Omega}.$$

In many cases, the above representation is not useful in practice since the expansion may involve infinitely many terms. Thus, we need an appropriate approximation. One possibility is to use the underlying MRA and the corresponding (bi-)orthogonal projection, namely

$$f_j := P_j f := \sum_{\mathbf{k} \in \mathcal{I}_j^{2D}} c_{j,\mathbf{k}} \varphi_{j,\mathbf{k}}, \quad c_{j,\mathbf{k}} := (f, \tilde{\varphi}_{j,\mathbf{k}})_{0;\Omega}, \quad \mathcal{I}_j^{2D} = \{0, \dots, 2^j - 1\}^2,$$

where  $\Phi_j = \{\varphi_{j,\mathbf{k}} : \mathbf{k} \in \mathcal{I}_j^{2D}\}$  is a basis for the multiresolution space  $\mathcal{S}_j^{2D}$ . As we have seen above, the approximation error  $\|f - P_j f\|_{0;\square}$  mainly depends on the regularity of the function  $f$  to be approximated (assuming that we have chosen the scaling function system appropriately).

Note however, that still we are facing a problem for a real application. In fact, the coefficients  $c_{j,\mathbf{k}}$  involve an integral which typically cannot be computed exactly. Of course, one can resort to quadrature formulae which typically involve point values of  $f$  and the dual scaling functions  $\tilde{\varphi}_{j,\mathbf{k}}$ . In most cases, point values of  $\tilde{\varphi}_{j,\mathbf{k}}$  cannot be computed exactly. One alternative is a quasi-interpolation scheme. Since we use a tensor product construction, we describe just the 1D-case in the sequel. The generalization to 2D is straightforward by the tensor product.

**Quasi-Interpolation.** A quasi-interpolation scheme produces an approximation of a given function  $f$  by only using point values of the function. This is similar to a classical interpolation. The difference is that a quasi-interpolation does not need to match point values of  $f$  at given nodes. This allows error estimates in  $L_2$  also with high orders of accuracy. Moreover, the well-known oscillations in standard interpolation can be avoided.

Often, the following approximation is used (see, e.g. [4, 14])

$$c_{j,k} \approx 2^{-\frac{j}{2}} f(2^{-j}k).$$

Obviously, this corresponds to approximate the integral for the true coefficient by a quadrature using only one point.

To increase the order of accuracy for the approximation, one has to use more than just one node. This results in a quasi-interpolation scheme of the form

$$c_{j,k} \approx \bar{c}_{j,k} := 2^{-\frac{j}{2}} \sum_{\ell=-m}^m \gamma_{d,\ell} f(2^{-j}(k+\ell))$$

with  $m := \lfloor \frac{d-1}{2} \rfloor$  and weights  $\gamma_{d,\ell}$ . These weights are determined in order to obtain a maximal order of accuracy. We refer to [1] for the construction of the weights and its values.

If we assume that  $f$  is only given on a bounded domain (e.g.  $\Omega \subset \square$ ), then the above formula requires point-values of  $f$  outside  $\Omega$ . This is typically done by extrapolating data or by extending the function  $f$  outside  $\Omega$ . In our main application, we know the true  $f$  so that this can in fact be done. In case of measurements of an optical surface, we will use the error of the measurements with respect to a true surface so that we can extrapolate the data by zero outside  $\Omega$  without loss of accuracy.

For the arising quasi-interpolant defined by

$$P_j^{\text{qi}} f := \sum_{k \in \mathcal{I}_j} \bar{c}_{j,k} \varphi_{j,k}$$

the following error estimate is known [22],

$$\|f - P_j^{\text{qi}} f\|_{0;\Omega} \lesssim 2^{-js} \|f\|_{-s;\mathbb{R}}, \quad (4.1)$$

i.e., the same order of approximation as  $P_j$ .

**5. Ray Tracing.** One typical application in optics is ray tracing, i.e., the calculation of light rays through a system of optical surfaces. In this section, we describe how to use the above multiresolution approximation and the corresponding wavelet representation in order to perform an efficient ray trace algorithm.

**5.1. Intersection and Refraction.** The following procedure for ray tracing is based on [17] and is adapted to the use of our B-spline representation of the surface. We define a ray  $\mathbf{r} : \mathbb{R} \rightarrow \mathbb{R}^3$  through a point  $\mathbf{p} = (p_x, p_y, p_z)^T \in \mathbb{R}^3$  in a direction  $\mathbf{d} = (d_x, d_y, d_z)^T \in \mathbb{R}^3$  as

$$\mathbf{r}(\alpha) := \mathbf{p} + \alpha \mathbf{d}, \quad \alpha \in \mathbb{R}.$$

Let us describe the refraction of such a ray by an optical surface given in terms of a function  $g$  (which could also be an approximation e.g. determined by a quasi-interpolation). First we need the point in which the ray intersects the surface. Let

us denote this point by  $\mathbf{x} = \mathbf{x}(x, y) = (x, y, g(x, y))^T \in \mathbb{R}^3$ ,  $(x, y) \in \Omega$ . The normal vector of the surface at  $\mathbf{x}$  is given as

$$\mathbf{n} = \mathbf{n}(x, y) = \mathbf{e}_1 \times \mathbf{e}_2 = (-\partial_x g(x, y), -\partial_y g(x, y), 1)^T, \quad (5.1)$$

where  $\mathbf{e}_1$  and  $\mathbf{e}_2$  are the two tangential vectors of the surface in  $\mathbf{x}$ , i.e.,  $\mathbf{e}_1 = \partial_x \mathbf{x}(x, y) = (1, 0, \partial_x g)^T$  and  $\mathbf{e}_2 = \partial_y \mathbf{x} = (0, 1, \partial_y g)^T$ . In order to obtain a unique intersection point, we have to assume that the ray is not parallel to the tangential plane. Then, the condition  $\mathbf{p} + \alpha \mathbf{d} = \mathbf{x}$  for the 3 unknowns  $\alpha$ ,  $x$  and  $y$  can be rephrased as

$$F(\alpha) := p_z + \alpha d_z - g(p_x + \alpha d_x, p_y + \alpha d_y) = 0, \quad F: \mathbb{R} \rightarrow \mathbb{R}.$$

This is obviously a one-dimensional nonlinear equation which can be numerically solved e.g. by Newton's method which requires the derivative

$$\begin{aligned} F'(\alpha) &= d_z - \partial_x g(p_x + \alpha d_x, p_y + \alpha d_y) d_x - \partial_y g(p_x + \alpha d_x, p_y + \alpha d_y) d_y \\ &= \mathbf{n}(x(\alpha), y(\alpha))^T \cdot \mathbf{d}, \end{aligned}$$

where  $x(\alpha) := p_x + \alpha d_x$  and  $y(\alpha) := p_y + \alpha d_y$ .

Now, we know the intersection point  $\mathbf{x}$  and the normal vector  $\mathbf{n}$  at this point. Let us denote by  $\gamma$  the incidence angle of the ray and the surface, i.e.  $\cos(\gamma) = \mathbf{n}^T \cdot \mathbf{d}$ , and by  $n, n'$  the refractive indices of the media in front of and behind the surface. So we can apply the *Law of Refraction*, i.e. in  $\mathbb{R}^3$ ,

$$\cos(\gamma') = \left( 1 - \left( \frac{n}{n'} \right)^2 (1 - \cos^2(\gamma)) \right)^{\frac{1}{2}},$$

to obtain the new incidence angle  $\gamma'$ . Hence, we can calculate the direction  $\mathbf{d}'$  of the ray in the medium behind the actual surface and proceed ray tracing with the next optical surface.

**5.2. Evaluation of the Quasi-Interpolation.** Let us now consider the case in which the parameterization of the surface is given in terms of the above described quasi-interpolant. Using tensor-product B-splines of order  $d$ , the approximation takes the form

$$(P_j^{\text{qi}} f)(x, y) = 2^j \sum_{\mathbf{k} \in \mathcal{I}_j^{2D}} \bar{c}_{j, \mathbf{k}} \cdot N_d(2^j x - k_1 + \frac{d}{2}) \cdot N_d(2^j y - k_2 + \frac{d}{2}), \quad (5.2)$$

with an index set  $\mathcal{I}_j^{2D} := \mathcal{I}_j \times \mathcal{I}_j$  and  $\mathcal{I}_j := \{ \lfloor 2^j \cdot -\frac{d}{2} \rfloor, \dots, \lfloor 2^j \cdot +\frac{d}{2} \rfloor \}$ . Since highly efficient routines for evaluating B-splines are available and the index set  $\mathcal{I}_j^{2D}$  is finite, the evaluation of (5.2) can be done efficiently as well. The same holds for derivatives of B-splines, so the calculation of partial derivatives of (5.2) is straightforward.

**6. Numerical Results for Representation and Ray Tracing.** In this section, we describe our numerical results concerning the multiresolution approximation of optical surfaces and the corresponding ray tracing. We use aspheres with a sufficiently large support in order to avoid extension at the boundaries. The ultimate goal is a sufficiently accurate approximation. All described schemes have been implemented within **FLENS**<sup>1</sup>. In order to test the performance within a realistic framework, we

<sup>1</sup>Flexible Library for Efficient Numerical Solutions, University of Ulm, Institute for Numerical Mathematics and Scientific Computing Center Ulm (UZWR), <http://flens.sourceforge.net>.

compare our above described ray trace algorithm with the optical design software **OASE**<sup>2</sup>. Further examples, in particular concerning surfaces that need extension methods on the boundary, are described in [13].

**6.1. Approximation of Optical Surfaces.** We start by describing numerical experiments for approximating a given optical surface in terms of a multiresolution approximation. The left part of Figure 6.1 shows a contour-color plot of the asphere  $S_1$  given by the parameterization

$$f_{S_1}(x, y) := \frac{\rho_x x^2 + \rho_y y^2}{2} + c_1 x + c_2 y + c_3 x^2 + c_4 xy + c_5 y^2 + c_6 x^3 + \dots$$

with parameters shown in Table 6.1. Note that the above numbering of the coefficients  $c_k$  is the standard labeling in optics.

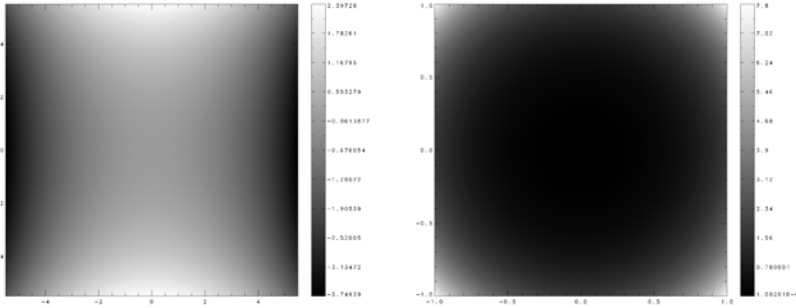


FIGURE 6.1. Contour-color plot of the test surfaces  $S_1$  (left) and  $S_2$  (right).

	$S_1$		$S_2$
$\rho_x$	$-2,15e^{-1}$	$\rho$	1,00
$\rho_y$	$1,22e^{-1}$		
$c_{10}$	$-4,05e^{-4}$	$c_1$	1,50
$c_{12}$	$-8,13e^{-4}$	$c_2$	$-7,00e^{-1}$
$c_{14}$	$5,73e^{-4}$	$c_3$	$5,00e^{-1}$
$c_{21}$	$-4,59e^{-6}$	$c_4$	$-5,00e^{-1}$
$c_{23}$	$1,14e^{-5}$		
$c_{25}$	$9,64e^{-6}$		
$c_{27}$	$4,45e^{-7}$		
$c_{36}$	$-2,69e^{-9}$		
$c_{38}$	$-7,96e^{-8}$		
$c_{40}$	$-8,79e^{-8}$		
$c_{42}$	$-9,16e^{-8}$		
$c_{44}$	$2,43e^{-8}$		

TABLE 6.1

Parameters of the test surfaces  $S_1$  and  $S_2$ ; all other coefficients  $c_k$  are zero.

We compute the approximation by the quasi-interpolation method described in §4.1 above. To use our method, a simple transformation from the bounding box of the asphere  $\Omega := [-5.5, 5.5]^2$  to the unit square is done. For different levels  $j$  and B-spline

<sup>2</sup>Optische Analyse und Synthese, Carl Zeiss AG.

orders  $d$ , we compute the root mean square value  $\text{RMS}(E_j)$  of the error  $e := f - P_j^{\text{qi}} f$ , where

$$E_j := \left( e(x_i, y_j) \right)_{i,j=1,\dots,n},$$

is a  $n \times n$  matrix and  $\{(x_i, y_j) : i, j = 1, \dots, n\}$  defines an equidistant mesh in  $\Omega$ . The RMS-value is defined as usual.

We list the corresponding errors  $\text{RMS}(E_j)$  of the surface  $S_1$  in the left part of Figure 6.2 for B-spline orders  $d = 1, \dots, 6$ , where we have used  $n = 10^4$ . The legend additionally shows the exponent  $s$  of the rate of convergence, i.e.,  $2^{-js}$ , see (4.1). For two levels  $j_1 < j_2$ , the exponent  $s$  is calculated by

$$s = \frac{1}{j_2 - j_1} \log_2 \left( \frac{\text{RMS}(E_{j_1})}{\text{RMS}(E_{j_2})} \right), \quad \text{if } \text{RMS}(E_{j_1}) > 0, \text{RMS}(E_{j_2}) > 0.$$

In the actual examples we used levels  $j_1 = 4$  and  $j_2 = 9$  to compute  $s$ .

We see that we reach machine accuracy for orders  $d = 5, 6$  and levels  $j \geq 10$ . Besides the case  $d = 5$ , we obtain the expected rate of convergence of  $s = d$ . This shows in particular that the analyzed surface is quite smooth. For  $d = 5$ , we obtain a super-convergence, namely  $s = 5.7$ . We have verified this also with other surfaces but do not have a clear explanation for this effect.

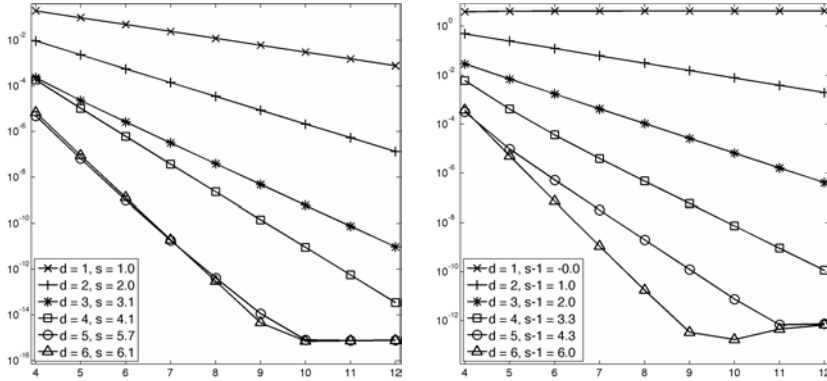


FIGURE 6.2. RMS error of the multiresolution approximation of  $S_1$  (left) and of the partial derivative  $\partial_x P_j f_{S_2}$  (right).

The second example concerns a rotationally symmetric asphere defined by

$$f_{S_2}(h) := \frac{\rho h^2}{2} + \sum_{k=2}^{\infty} c_k h^{2k},$$

where  $h^2 := x^2 + y^2$ . The coefficients are detailed in Table 6.1 and a contour-plot is shown in the right part of Figure 6.1. We have used this example in order to investigate the approximation order of the first derivative, where we expect to lose one order of approximation. Hence, we compute  $E_j$  as above, where now

$$e := \frac{\partial}{\partial x} \left( f - P_j^{\text{qi}} f \right).$$

We obtain the error  $\text{RMS}(E_j^{S_2})$  in the right part of Figure 6.2. As above, the legend shows the exponent of the rate of convergence which is here in the order of  $2^{-j(s-1)}$ .

As we see, we obtain the expected rate  $s = d - 1$  for  $d = 1, 2, 3$ . Starting from  $d = 4$ , the rate is larger than  $d - 1$  which is an indication for the smoothness of the surface. At a first glance, one might wonder why the error for  $d = 6$  and  $j > 9$  increases. Note, however, that the error is already in the order of  $10^{-12}$  so that the machine accuracy influences the computations.

**6.2. Accuracy of the Ray Tracing.** Next, we test the performance of the above described ray trace method. For a given set of rays  $\mathbf{r}_i, i = 1, \dots, n$ , we compute the intersection point  $\mathbf{x}_i$  and the normal  $\mathbf{n}_i$ . Again, we use **OASE** to validate our results. Of course, both intersection and normal depend on the level  $j$  so that we use the notation  $\mathbf{x}_i^{(j)}$  and  $\mathbf{n}_i^{(j)}$ . By  $\mathbf{x}_i^{(0)}$  and  $\mathbf{n}_i^{(0)}$ , we indicate the results computed by **OASE**.

For  $n = 10^6$  rays, we report the maximal deviation of all rays

$$M_{\mathbf{x},j} := \max_{i=1,\dots,n} \left\{ \|\mathbf{x}_i^{(0)} - \mathbf{x}_i^{(j)}\| \right\}, \quad M_{\mathbf{n},j} := \max_{i=1,\dots,n} \left\{ \|\mathbf{n}_i^{(0)} - \mathbf{n}_i^{(j)}\| \right\},$$

where  $\|\cdot\|$  denotes the standard Euclidean norm in  $\mathbb{R}^3$ . The error plot for surface  $S_1$  is given in the left part of Figure 6.3. We use  $\varepsilon = 10^{-12}$  for the stopping criterion of Newton's method and the parameter  $s$  is computed based on levels 4 and 7. In the right part of Figure 6.3, we indicate the error  $M_{\mathbf{n},j}$  for computing the normal vector.

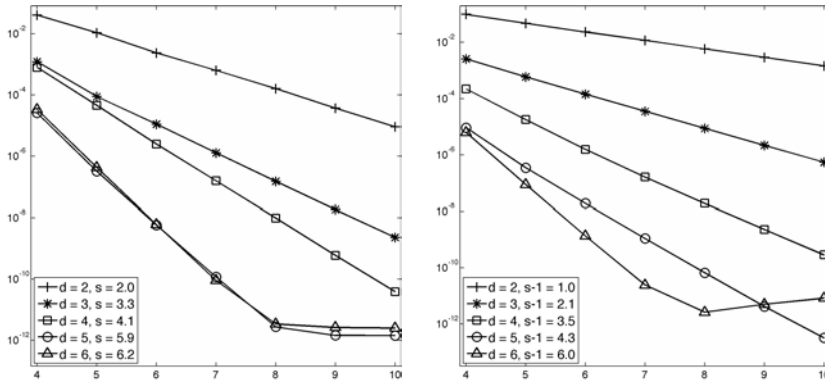


FIGURE 6.3. Maximal deviation  $M_{\mathbf{x},j}$  of the intersection point (left) and  $M_{\mathbf{n},j}$  of the normal (right).

We observe a similar behavior as above. The rate of convergence for  $M_{\mathbf{x},j}$  is  $s \approx d$ , again with a super-convergence for  $d = 5$ . Since the normal is based on derivatives, it is not surprising that we obtain  $s \approx d - 1$ , but again increasing for larger  $d$ .

**7. Wavelet Analysis and Correction.** In this section, we describe the use of wavelet methods to analyze and correct given real and synthetic optical surfaces.

To analyze the perturbation of an asphere on a circular aperture  $\Omega_{\text{asphere}} = \{(x, y) : x^2 + y^2 \leq 1\}$  we inscribe the circle into a square  $\Omega := [-1, 1]^2$  and use a tensor product periodic FWT on  $\Omega$ .

We want to define PSD errors on arbitrary disks and toruses. Therefore we fix an inner and outer radius  $r_i, r_o$  and a decay length  $l \geq 0$ . To get smooth edges we now

multiply  $err_{\text{PSD}}$  by the rotationally symmetric infinitely differentiable decay function

$$dec_{r_i, r_o, l}(x, y) := \begin{cases} 0, & \text{if } h = 0.0, \\ 1, & \text{if } h \geq l, \\ \left(1 + e^{5 \cdot \tan\left(\frac{\pi}{2} - \frac{\pi}{l} h\right)}\right)^{-1}, & \text{else,} \end{cases}$$

for inner points  $(x, y) \in \{(x, y) \in \mathbb{R}^2 : r_i \leq r \leq r_o\}$ , where  $r := \sqrt{x^2 + y^2}$ , and the distance  $h := \min\{r_o - r, r - r_i\}$  to the nearest boundary. The univariate function  $dec_{0,1,0.4}$  is shown in Figure 7.1.

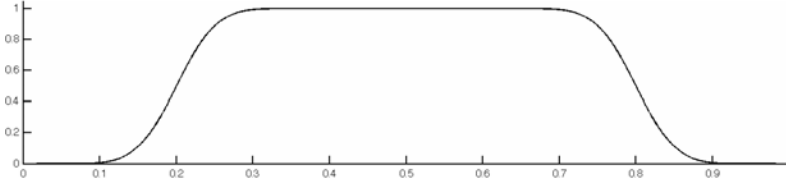


FIGURE 7.1. Decay function  $dec_{0,1,0.4}(x, 0)$ .

It is well-known that  $err_{\text{ZFR}}$  is not zero on the boundary  $\partial\Omega_{\text{asphere}}$  which is a consequence of the particular model for the ZFR error. However, we want to study the error in the inner part of the surface, since in practice most of the light passes through here. Thus, we also multiply the ZFR error with the above decay function  $dec_{r_i, r_o, l}$  for fixed  $r_i = -l$  and  $r_o = 1$ .

**7.1. Localization of Mid Spatial Frequency Perturbed Domains.** If a manufactured surface has a significant mid spatial frequency perturbation (i.e., a PSD-error), the surface usually does not meet the desired specification. Especially when the surface has a shape with steep regions, the performance of the optical system can be seriously affected by the presence of a PSD-error. In that case, a costly *Computer Controlled Polishing (CCP)* is needed. It would be desirable to perform a CCP only in regions where it is really needed. We want to use a wavelet analysis to detect such local perturbations.

Again, we use synthetic data in order to simulate localized mid spatial frequency errors. Therefore we split the domain  $\Omega_{\text{asphere}}$  into two parts, namely

$$\Omega_{\text{int}} := \left\{ (x, y) : \sqrt{x^2 + y^2} \leq 0.5 \right\}, \quad \Omega_{\text{ext}} := \left\{ (x, y) : 0.5 < \sqrt{x^2 + y^2} \leq 1.0 \right\},$$

i.e.,  $\Omega_{\text{asphere}} = \Omega_{\text{int}} \cup \Omega_{\text{ext}}$ . We assume that the specification of the surface is satisfied in the interior  $\Omega_{\text{int}}$ , whereas we do not make any assumptions for  $\Omega_{\text{ext}}$ . To obtain smooth edges of the PSD-errors we use the decay function  $dec_{r_i, r_o, 0.3}$  for the data with corresponding radii. In addition to localized PSD-errors we also add low spatial frequency errors in terms of a ZFR-error. This is done to obtain a more realistic model of a surface. An example with  $n_{\text{int}} = n_{\text{ext}} = 51$  and  $\text{RMS}(err_{\text{PSD}}|_{\Omega_{\text{int}}}) = 1.0 \cdot 10^{-4}$ ,  $\text{RMS}(err_{\text{PSD}}|_{\Omega_{\text{ext}}}) = 2.0 \cdot 10^{-4}$  is shown in the left part of Figure 7.2.

Starting from the single-scale representation in terms of the above described quasi-interpolation, we compute the wavelet representation

$$Q_j^{\text{qi}} f = \sum_{l=0}^{j-1} \sum_{e \in \{\text{H, V, D}\}} \sum_{\mathbf{k}} \bar{d}_{l, \mathbf{k}}^e \psi_{l, \mathbf{k}}^e, \quad \mathbf{k} \in \mathcal{J}_\ell^e,$$

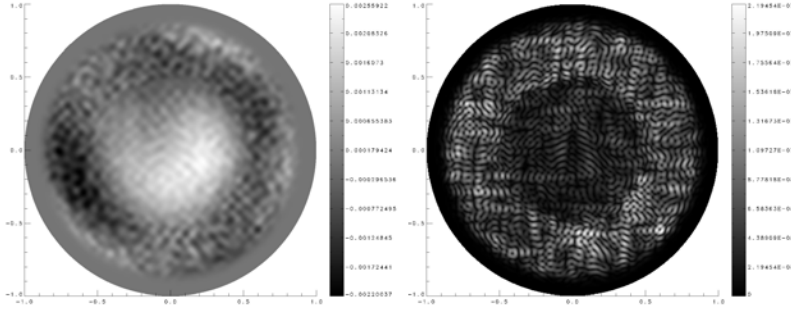


FIGURE 7.2. Surface with fixed ZFR-error and varying PSD-errors (left) and aggregated detail  $\mathbf{w}_9$  for orders  $d = \bar{d} = 3$  (right).

like in §2. Next, in order to make the detail pattern clearly visible, we aggregate the different parts of the detail and compute

$$\mathbf{w}_\ell = (w_{\ell,\mathbf{k}})_{\mathbf{k} \in \mathcal{J}_\ell^*} := \sqrt{(d_{\ell,\mathbf{k}}^V)^2 + (d_{\ell,\mathbf{k}}^H)^2 + (d_{\ell,\mathbf{k}}^D)^2}. \quad (7.1)$$

Note that due to periodicity we have  $|\mathcal{I}_j^{2D}| = 2^{2j}$  and  $|\mathcal{J}_\ell^V| = |\mathcal{J}_\ell^H| = |\mathcal{J}_\ell^D| = 2^{2j}$  so that we can use the same index set  $\mathcal{J}_\ell^*$  for all 3 parts of the detail. Due to the Riesz basis property, the quantity  $\|\mathbf{w}_\ell\|_{\ell_2(\mathcal{J}_\ell^*)}$  is equivalent to  $\|Q_j^{qi} f\|_{0;\Omega}$  which represents the energy of error. In the right part of Figure 7.2 we show a contour-color plot of  $\mathbf{w}_9$ . We can clearly see local effects that allow to restrict a CCP to these regions only.

Next, we use a simulation for a PSD-error with varying waviness. We do this by using different parameters  $n$  in the model of the PSD-error, namely  $n_{int} = 51$  and  $n_{ext} = 61$ . We illustrate such an example in Figure 7.3, where we use equal RMS-values for both domains, namely  $\text{RMS}(err_{\text{PSD}}|_{\Omega_{int}}) = \text{RMS}(err_{\text{PSD}}|_{\Omega_{ext}}) = 1.0 \cdot 10^{-4}$ . In the right part of Figure 7.3 we show a contour-color plot of  $\mathbf{w}_9$ . Again, we can

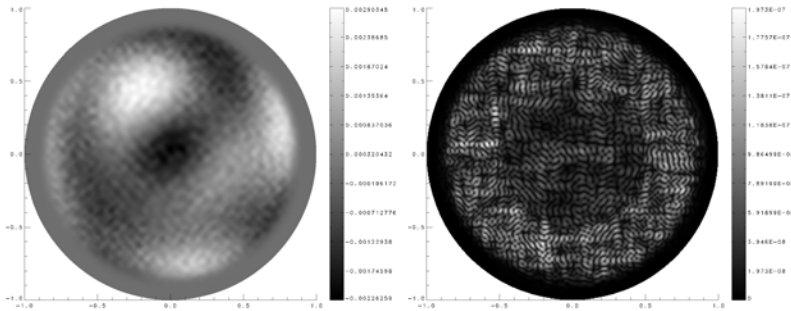


FIGURE 7.3. Surface with  $n_{int} \neq n_{ext}$  (left) and detail  $\mathbf{w}_9$  for  $d = \bar{d} = 3$  (right).

clearly see the localization of the PSD error in the exterior  $\Omega_{ext}$ .

**7.2. Error Separation of Manufactured Surfaces.** Let us now consider the case where a manufactured surface is given, its theoretical shape is known and we would like to analyze the errors as described above. So far, in optics typical low frequency errors as well as optical aberrations are well described by Zernike polynomials. Hence, one is interested in expanding the manufacturing error of a surface in

such a representation. Thus, the goal is to minimize the mid and high spatial frequencies. In the multiscale representation in terms of wavelets this means that low spatial frequency perturbations occur on other levels than mid and high spatial frequency perturbations.

**7.2.1. Comparison of Thresholding and Truncation.** To this end, we investigate if we can associate  $err_{\text{ZFR}}$  and  $err_{\text{PSD}}$  to certain ranges of levels, in that case truncation and thresholding methods should perform almost equal. In order to do so, we analyze various realizations of the two errors and do a wavelet decomposition up to level  $j = 6$ . Let us denote by  $d_{j,\mathbf{k}}^{\text{trunc}}$  and  $d_{j,\mathbf{k}}^{\text{thresh}}$  the wavelet coefficients arising from truncation at level  $j_{\text{trunc}}$  or (hard-)thresholding with a threshold  $T \in \mathbb{R}_+$ , i.e.,

$$d_{j,\mathbf{k}}^{\text{trunc}} := \begin{cases} 0, & \forall j \geq j_{\text{trunc}}, \\ d_{j,\mathbf{k}}, & \text{else,} \end{cases} \quad d_{j,\mathbf{k}}^{\text{thresh}} := \begin{cases} 0, & \text{if } |d_{j,\mathbf{k}}| \leq T, \\ d_{j,\mathbf{k}}, & \text{else.} \end{cases}$$

Accordingly, let the projectors be defined by

$$Q_j^{\text{trunc}} f = \sum_{\mathbf{k} \in \mathcal{J}_j^{2D}} d_{j,\mathbf{k}}^{\text{trunc}} \psi_{j,\mathbf{k}}, \quad Q_j^{\text{thresh}} f = \sum_{\mathbf{k} \in \mathcal{J}_j^{2D}} d_{j,\mathbf{k}}^{\text{thresh}} \psi_{j,\mathbf{k}}.$$

In order to compare a level-wise truncation with a thresholding, we simulate different  $err_{\text{TOTAL}}$  with varying amount of  $err_{\text{PSD}}$  to study the influence of the PSD-error on this separation of levels and compute the relative error of the reconstruction to the optimal ZFR-surface  $err_{\text{ZFR}}$  after the manipulation. As in §6.1 we approximate the  $L_2$ -norm by the RMS-value and compute

$$\rho^* \approx \frac{\|Q_j^* f - err_{\text{ZFR}}\|_{0;\Omega}}{\|err_{\text{TOTAL}} - err_{\text{ZFR}}\|_{0;\Omega}}.$$

In Table 7.1, we show the above defined ratio as an average over  $N = 100$  realizations, i.e.,

$$\bar{\rho}^* := \frac{1}{N} \sum_{i=1}^N \rho_i^*,$$

where  $\rho_i^*$  denotes the ratio for the  $i$ -th realization and we used orders  $d = 3, \tilde{d} = 9$ . By varying the parameter  $n$  in the simulation of the PSD as described in §3, we vary the frequencies present in  $err_{\text{PSD}}$ .

RMS( $err_{\text{PSD}}$ ) (* · 10 <sup>-4</sup> )	$n = 31$		$n = 51$		$n = 71$		$n = 91$	
	A	B	A	B	A	B	A	B
2.0	64.2	64.8	48.8	50.9	39.7	43.3	34.2	36.6
4.0	53.0	53.8	36.9	37.0	29.8	30.1	26.0	26.6
8.0	38.1	38.6	30.4	30.9	24.2	24.3	19.9	20.0
16.0	28.4	29.0	20.9	20.2	18.1	18.3	16.1	16.4

TABLE 7.1

Comparison of thresholding  $\bar{\rho}^{\text{thresh}}$  (A) and truncation  $\bar{\rho}^{\text{trunc}}$  (B) in percent for orders  $d = 3, \tilde{d} = 9$ .

We observe no significant difference between truncation and thresholding which has the above mentioned interpretation. For increasing  $n$ , we observe decreasing  $\bar{\rho}$  which was expected since the separation of low and mid frequency part of the error is more pronounced.

**7.2.2. Estimation of the Truncation Level.** As we have seen by our above described experiments, the wavelet decomposition allows a separation of low and mid spatial frequency errors via a level-wise truncation. Of course, for given data it is not obvious how to choose the optimal truncation level  $j_{\text{trunc}}$ . Now, we describe a deterministic approach to determine  $j_{\text{trunc}}$ .

It is well-known that

$$\hat{\sigma}^2(\mathbf{x}) := \frac{1}{n-1} \sum_{k=1}^n (x_k - \bar{x})^2, \quad \bar{x} := \frac{1}{n} \sum_{k=1}^n x_k,$$

is an estimator for the variance of a vector  $\mathbf{x} = (x_1, \dots, x_n)^T \in \mathbb{R}^n$ . We use this estimator now for  $\mathbf{w}_\ell$  defined in (7.1), i.e.  $\hat{\sigma}_\ell^2 := \hat{\sigma}^2(\mathbf{w}_\ell)$ . If we normalize the scaling functions in  $L_1$ , i.e.,  $\|\varphi_{j,k}\|_{L_1} \sim \|\varphi\|_{L_1}$ , the values of  $\hat{\sigma}_\ell^2$  should be comparable for different values of  $\ell$ , see [4]. Since ZFR- and PSD-error appear on different levels, there should be a discrete local minimum in the sequence  $\hat{\sigma}_\ell^2$ ,  $\ell = 1, \dots, j-1$ . The corresponding level separates the involved level ranges and can be used as truncation level  $j_{\text{trunc}}$ .

In order to investigate the performance of this approach, we fix a maximum level  $j = 10$  and simulate 100 randomly generated surfaces. We compare an optimal truncation by computing all possible truncations with the truncation induced by the approximate level  $j_{\text{trunc}}$  determined above. In Table 7.2, we show as above the relative error of the reconstruction for different values  $n$  indicating the waviness. For the relevant cases of high waviness we obtain a very good agreement of optimal and approximated truncation.

RMS( $err_{\text{PSD}}$ ) (* · 10 <sup>-4</sup> )	$n = 31$		$n = 51$		$n = 71$		$n = 91$	
	A	B	A	B	A	B	A	B
2.0	63.9	71.3	49.3	79.3	42.6	45.7	35.9	36.3
4.0	54.0	56.0	36.9	37.2	29.6	30.0	25.8	28.8
8.0	38.5	76.9	30.9	40.2	24.4	27.8	19.9	21.0
16.0	29.2	86.7	21.2	71.6	18.3	58.6	16.3	37.4

TABLE 7.2

Comparison of optimal  $\bar{\rho}^{\text{opt}}$  (A) and approximated  $\bar{\rho}^{\text{app}}$  (B) truncation in percent for level  $j = 10$  and orders  $d = 3$ ,  $\bar{d} = 9$ .

**7.2.3. Example for the Separation of Low and Mid Frequencies.** Let us show an example for the separation of low and mid spatial frequency perturbation by our wavelet method. We start by a simulated surface having both ZFR- and PSD-error components, shown in the left part of Figure 7.4. Since we have used a simulation for the error, we can compare the original ZFR-error and the ZFR-part of the error as determined by our wavelet method. We show both quantities in Figure 7.5 and the point-wise difference in the right part of Figure 7.4. The maximal deviation is in the order of  $8.5 \cdot 10^{-4}$  which seems quite good. Moreover, we see that the location of the largest error terms is at the boundaries of the shape of the error functions. In order to avoid this, one could follow an adaptive strategy which is devoted to a forthcoming paper. Finally, we have performed a Zernike fit to 100 coefficients and get a RMS-error of  $6.6 \cdot 10^{-5}$  for the reconstructed data, while the RMS-error is  $1.0 \cdot 10^{-3}$  for the original surface.

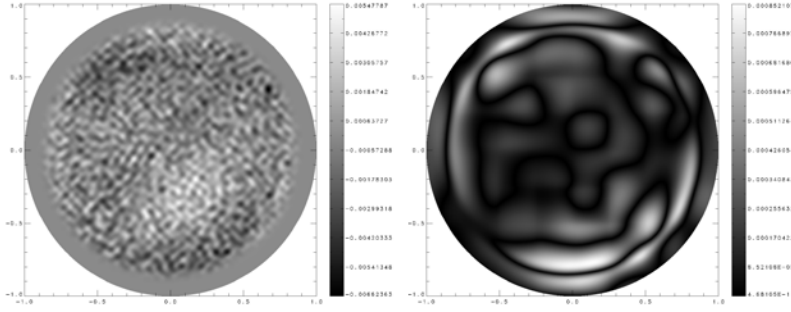


FIGURE 7.4. Simulation of a low and mid spatial frequency perturbed surface (left) and error  $|Q_j^{\text{trunc}} f - \text{err}_{\text{ZFR}}|$  of the wavelet reconstruction (right).

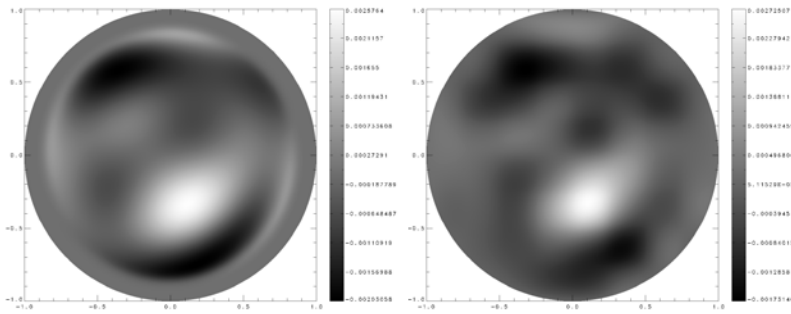


FIGURE 7.5. Original low spatial frequency perturbation (left) and reconstruction by the wavelet method (right),  $j = 10$ ,  $d = 3$ ,  $d = 9$ .

**7.3. Correction of Local Errors.** Finally, we use wavelets in order to detect and correct local errors of an optical surface. In Figure 7.6, we see on the top right part an artificial localized error that we add to measurements of a surface. The resulting surface is shown on the top left part of the same figure. On the bottom part of the figure, we show the aggregated wavelet detail for level  $\ell = 5$  (left) and  $\ell = 6$  (right). The first observation is the strong dominance of details close to the boundary. Note that this is *not* caused by the embedding of the circular domain  $\Omega$  into the square and using periodized wavelets there. Since we consider the error, these figures show that there is a true error close to the boundary. This fact can already be seen by the plot of the surface (top left). The explanation is that the true surface has a steep gradient close to the boundary where no light passes through. Therefore, errors in that area are in fact permitted in the production.

If we have a close look to the detail in level  $\ell = 6$ , we do see the local perturbation (which is not clearly visible on level  $\ell = 5$ ). This allows to correct this local deformation. Finally, one notices also a true local error in the center of the surface.

**8. Summary and Outlook.** In this paper, we introduced a wavelet method for representing, analyzing, simulating and correcting optical surfaces. The method consists of five steps, namely

1. Highly accurate B-spline quasi-interpolation of measured data.
2. Wavelet decomposition using biorthogonal B-spline wavelets (FWT).
3. Determination of a truncation level based on the wavelet coefficients.
4. Level-wise truncation of wavelet coefficients. Possible correction.

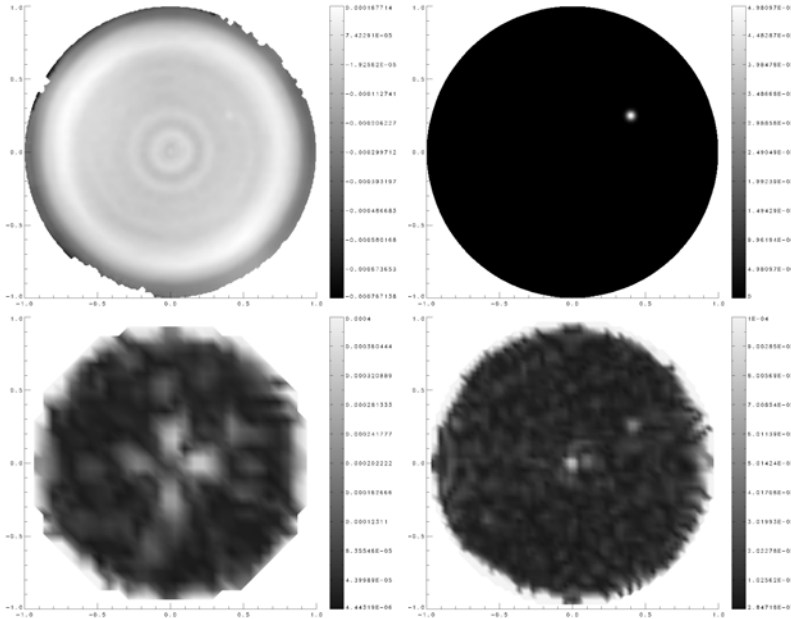


FIGURE 7.6. Surface with artificial error (top left), artificial local error (top right) and aggregated wavelet details for level 5, 6 (bottom) for  $j = 9$ ,  $d = 3$ ,  $\tilde{d} = 9$  and .

### 5. Wavelet reconstruction (IFWT).

We have shown the abilities of the proposed method for both real and synthetic data for optical surfaces. Since the theoretic shape of the surfaces under consideration is known, we can use the error of the surface for our wavelet method. This allows embedding of the layout of the surface into a square and use highly efficient wavelet methods there. In addition, we developed and implemented a ray tracing method based upon the wavelet representation of the surface. This method allows to simulate the behavior of the optical system, in particular the influence of occurring errors.

The positive results documented in this paper motivate us to continue with investigations concerning the use of wavelet methods in optics. One direction already mentioned above is the use of adaptive strategies. In fact, modern optical systems are highly sophisticated and consist of several lenses that may be arranged in a fairly complicated way. It is obviously of economical interest to minimize a posteriori polishing and correcting already manufactured surfaces. Thus, we aim at developing an adaptive wavelet minimization method that enables a given optical system to meet the desired specification with minimal corrections. We will report on this in a forthcoming paper.

### REFERENCES

- [1] K. BITTNER AND K. URBAN, *Adaptive wavelet methods using semiorthogonal spline wavelets: sparse evaluation of nonlinear functions*, Appl. Comput. Harmon. Anal., 24 (2008), pp. 94–119.
- [2] O. ÇAKMAKCI, B. MOORE, H. FOROOSH, AND J. P. ROLLAND, *Optimal local shape description for rotationally non-symmetric optical surface design and analysis*, Opt. Express, 16 (2008), pp. 1583–1589.

- [3] H. CHASE, *Optical design with rotationally symmetric NURBS*, vol. 4832, Proc. SPIE, 2002, pp. 10–24.
- [4] A. COHEN, *Wavelet methods in numerical analysis*, in Handbook of Numerical Analysis, Vol. VII, Handb. Numer. Anal., VII, North-Holland, Amsterdam, 2000, pp. 417–711.
- [5] A. COHEN, I. DAUBECHIES, AND J.-C. FEAUVEAU, *Biorthogonal bases of compactly supported wavelets*, Comm. Pure Appl. Math., 45 (1992), pp. 485–560.
- [6] C. DE BOOR, *A practical guide to splines*, vol. 27 of Appl. Math. Sci., Springer-Verlag, New York, revised ed., 2001.
- [7] A. DOGARIU, J. UOZUMI, AND T. ASAKURA, *Wavelet transform analysis of slightly rough surfaces*, Optics Communications, 107 (1994), pp. 1–5.
- [8] G. W. FORBES, *Shape specification for axially symmetric optical surfaces*, Opt. Express, 15 (2007), pp. 5218–5226.
- [9] G. G. GREGORY, E. R. FRENIERE, AND L. R. GARDNER, *Using spline surfaces in optical design software*, vol. 4769, Proc. SPIE, 2002, pp. 75–83.
- [10] A. W. GREYNOLDS, *Superconic and subconic surface descriptions in optical design*, vol. 4832, Proc. SPIE, 2002, pp. 1–9.
- [11] H. GROSS, ed., *Handbook of Optical Systems, Fundamentals of Technical Optics*, Wiley-VCH, 1st ed., 2005.
- [12] H. GROSS, H. ZÜGGE, M. PESCHKA, AND F. BLECHINGER, *Handbook of Optical Systems, Aberration Theory and Correction of Optical Systems*, Wiley-VCH, 1st ed., 2007.
- [13] P. JESTER, *Beschreibung optischer Grenzflächen mit Wavelets*, diploma thesis, Institute for Numerical Mathematics, University of Ulm, Germany, 2007.
- [14] S. MALLAT, *A wavelet tour of signal processing*, Academic Press Inc., San Diego, CA, 1998.
- [15] B. R. A. NIJBOER, *The diffraction theory of aberrations*, PhD thesis, University of Groningen, 1942.
- [16] P. OTT, *Optic design of head-up displays with freeform surfaces specified by NURBS*, vol. 7100, Proc. SPIE, 2008.
- [17] A. K. RIGLER AND T. P. VOGL, *Spline functions: an alternative representation of aspheric surfaces*, Appl. Opt., 10 (1971), pp. 1648–1651.
- [18] J. E. STACY, *Asymmetric spline surfaces: characteristics and applications*, Appl. Opt., 23 (1984), pp. 2710–2714.
- [19] C.-L. TIEN AND Y.-R. LYU, *Optical surface flatness recognized by discrete wavelet transform and grey level co-occurrence matrix*, Measurement Science and Technology, 17 (2006), pp. 2299–2305.
- [20] K. URBAN, *Wavelets in numerical simulation*, vol. 22 of Lect. Notes Comput. Sci. Eng., Springer-Verlag, Berlin, 2002. Problem adapted construction and applications.
- [21] ———, *Wavelet Methods for Elliptic Partial Differential Equations*, Oxford University Press, 2009.
- [22] V. A. ZHELUEDEV, *Local quasi-interpolation splines and Fourier transforms*, Dokl. Akad. Nauk SSSR, 282 (1985), pp. 1293–1298.